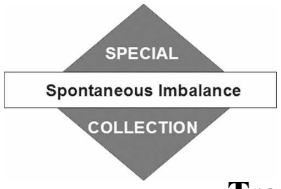

Tracking Gravity Waves in Baroclinic Jet-Front Systems

YONGHUI LIN

Department of Atmospheric Sciences, Texas A&M University, College Station, Texas, and State Key Laboratory of Severe Weather, Chinese Academy of Meteorological Sciences, Beijing, China

FUQING ZHANG

Department of Atmospheric Sciences, Texas A&M University, College Station, Texas

(Manuscript received 30 March 2007, in final form 9 October 2007)

ABSTRACT

Using a two-dimensional Fourier decomposition and a four-dimensional ray-tracing technique, the propagating characteristics and source mechanisms of mesoscale gravity waves simulated in idealized baroclinic jet-front systems are investigated. The Fourier decomposition successfully separates the simulated gravity waves from a complex background flow in the troposphere. Four groups of gravity waves in the lower stratosphere are identified from the spectral decomposition. One is a northward-propagating short-scale wave packet with horizontal wavelength of ~150 km, and another is a northeastward-propagating medium-scale wave packet with horizontal wavelength of ~350 km. Both of these are most pronounced in the exit region of the upper-tropospheric jet. A third group exists in the deep trough region above (and nearly perpendicular to) the jet, and a fourth group far to the south of the jet right above the surface cold front, both of which are short-scale waves and have a horizontal wavelength of ~100–150 km.

Ray-tracing analysis suggests that the medium-scale gravity waves originate from the upper-tropospheric jet-front system where there is maximum imbalance, though contributions from the surface fronts cannot be completely ruled out. The shorter-scale, northward-propagating gravity waves in the jet-exit region, on the other hand, may originate from both the upper-tropospheric jet-front system and the surface frontal system. The shorter-scale gravity waves in the deep trough region across the jet (and those right above the surface cold fronts) are almost certain to initiate from the surface frontal system. Ray-tracing analysis also reveals a very strong influence of the spatial and temporal variability of the complex background flow on the characteristics of gravity waves as they propagate.

1. Introduction

The generation and propagation of gravity waves are essential and important dynamic processes within the atmosphere, and many studies have yielded a more thorough understanding of their origins and general characteristics (Fritts and Alexander 2003). Gravity waves play a prominent role in transferring large amounts of energy and momentum, which can have significant impact on the general circulation of the atmosphere (e.g., Holton and Alexander 2000). They also can initiate and organize convection (e.g., Zhang et al. 2001), and they are identified as a possible source of clear-air turbulence (e.g., Koch et al. 2005). Mountains, convection, wind shear, and adjustment of unbalanced flows related to jet streams and frontal systems are the most important sources of gravity waves (Hooke 1986).

Uccellini and Koch (1987) conceptualized the synoptic pattern of gravity wave generation and found that mesoscale waves with amplitudes of 1–15 hPa, horizontal wavelengths of 50–500 km, and periods of 1–4 h frequently appear in the vicinity of jet streaks and on the cold-air side of surface frontal systems. Since frontal systems and other related synoptic systems play an important role in the generation of the gravity waves, the origin of gravity waves accompanying low-level and upper-level frontogenesis has been investigated with the use of idealized models (e.g., Snyder et al. 1993; Griffiths and Reeder 1996). Snyder et al. (1993) found that gravity waves with a 100–200-km wavelength may be emitted by frontogenesis when the cross-front scale be-

Corresponding author address: Dr. Fuqing Zhang, Department of Atmospheric Sciences, Texas A&M University, College Station, TX 77845-3150.
E-mail: fzhang@tamu.edu

DOI: 10.1175/2007JAS2482.1

comes sufficiently small. Meanwhile, Griffiths and Reeder (1996) found that propagating gravity waves with horizontal wavelengths of order 400–1200 km can be generated from upper-level frontogenesis.

Using a three-dimensional hemispheric primitive equation model, O'Sullivan and Dunkerton (1995) demonstrated that gravity waves arose spontaneously as the tropospheric jet stream was distorted by baroclinic instability. With a multiply nested mesoscale model with grid spacing down to 3.3 km, Zhang (2004, hereafter Z04) further investigated the generation of *mesoscale* gravity waves during the life cycle of idealized baroclinic jet-front systems. Long-lived, vertically propagating gravity waves with horizontal wavelengths of ~100–200 km are simulated near the exit region of the upper-tropospheric jet streaks, consistent with past observational studies (Uccellini and Koch 1987). Most recently, Plougonven and Snyder (2005), Plougonven and Zhang (2007), and Wang and Zhang (2007) examined the gravity wave generation during different life cycles of baroclinic waves.

The imbalance diagnosis and model simulations in Z04 suggest that spontaneous balance adjustment is likely the mechanism responsible for the generation of these gravity waves. This is a generalization of geostrophic adjustment, which is a theoretical simplification of a generally more complex process. The role of synoptic-scale imbalance in generating mesoscale gravity waves were further examined most recently in Plougonven and Zhang (2007). However, as noted in Lane et al. (2004), without a sophisticated wave source analysis it is often difficult to determine unambiguously whether mesoscale structures, such as jets and upper-level fronts, are the source of the gravity waves or a response to some other forcing that also generates the waves.

The ray-tracing technique has been widely used to investigate gravity wave sources and the influence of the background atmosphere on the spatial and temporal variability of gravity wave activity (e.g., Jones 1969; Lighthill 1978). Dunkerton and Butchart (1984) developed a simple ray-tracing model for gravity waves and found that longitudinal asymmetry in the background flow led to "forbidden" regions into which stationary gravity waves with horizontal wavelengths of 50 ~ 200 km could not propagate. Eckermann (1992) developed a numerical ray-tracing model to trace gravity waves in a realistic zonal-mean atmosphere. Marks and Eckermann (1995) extended the ray-tracing formalism to include zonal variability and to accommodate internal gravity waves of all frequencies in a rotating, stratified, compressible, and three-dimensional atmosphere.

The purpose of the present study is threefold. First, the characteristics of mesoscale gravity waves simulated by Z04 are examined using a two-dimensional Fourier decomposition method. Second, potential sources of the above gravity waves are identified using a four-dimensional ray-tracing numerical model and the Fourier decomposition. Finally investigated is the influence of the four-dimensional varying background flow (i.e., the propagating media) on gravity wave characteristics such as frequency and wavelength as well as on group propagation trajectories.

The present paper is arranged as follows: Section 2 gives a brief introduction of the ray-tracing model and background data resources used in this study. An overview of the characteristics of mesoscale gravity waves simulated in Z04 is revisited in section 3. Section 4 describes wave identification and characteristics from the 2D Fourier spectral decomposition. Section 5 presents the results of ray tracing and reverse ray tracing the gravity waves. The impacts of initial gravity wave parameters on the ray-tracing results are analyzed in section 6. Finally, conclusions and discussion are given in section 7.

2. The ray-tracing model

The Gravity Wave Regional or Global Tracer (GROGRAT) model developed in Marks and Eckermann (1995) and Eckermann and Marks (1997) is used in this study to track the propagation and amplitude evolution of gravity waves. GROGRAT computes gravity wave group trajectories through gridded numerical representations of the background atmosphere, using a fully nonhydrostatic dispersion relation containing both rotation and density stratification, accounting for refraction due to three-dimensional spatial gradients and time variations in the background atmosphere. Wave amplitudes are tracked along ray paths using a somewhat simplified form of the wave action continuity equation that accounts only for vertical compression/dilation of wave action densities (Marks and Eckermann 1995). More general wave action conservation calculations using spatial ray methods require multiple rays or extra so-called derived ray equations can be found in Broutman et al. (2001).

GROGRAT has been used by many investigators to trace gravity waves through different gridded numerical representations of the atmosphere (e.g., Guest et al. 2000; Broutman et al. 2001; Gerrard et al. 2004). For the Wentzel–Kramers–Brillouin (WKB) assumptions used in deriving the ray-tracing equations to be valid, the spatial derivatives of the background atmospheric parameters must vary smoothly during numerical integra-

tion. The following parameter (hereafter referred to as WKB index),

$$\delta = \frac{1}{m^2}\left|\frac{\partial m}{\partial z}\right| \approx \left|\frac{1}{c_{gz}m^2}\frac{dm}{dt}\right|, \qquad (1)$$

is introduced to ensure the validity of the WKB approximations, where m is vertical wavenumber, C_{gz} is vertical group velocity, and a given ray integration is terminated if $\delta \geq 1$ [see (5) of Marks and Eckermann (1995); Broutman (1984)].

3. Overview of gravity waves simulated in Z04

This study further examines the source mechanisms and characteristics of the gravity waves initiated from a developing baroclinic jet-front system simulated in the control experiment (CNTL) of Z04. The idealized simulation in Z04 uses the fifth-generation Pennsylvania State University–National Center for Atmospheric Research Mesoscale Model (MM5). Three two-way-nested model domains (D1, D2, and D3) respectively use 90-, 30-, and 10-km horizontal grid spacing, and 60 vertical layers are used with 360-m vertical spacing. D1 is configured in the shape of a channel 27 000 km long (x direction) and 8010 km wide (y direction), and D2 (D3) is a rectangular subdomain 9300 (3100) km long and 4500 (2500) km wide centered at $x = 6150$ (17 000) km and $y = 2850$ (6700) km within D1 (D2). Radiative top boundary conditions are employed for all model domains, and moist processes, surface fluxes, and friction are all neglected in the simulations. For this study, GROGRAT uses as its background atmosphere the 30-km (D2) output of the control simulation of Z04, but the simulated data are coarsened to 60-km (0.5-km) horizontal (vertical) grids. This coarsened output is further smoothed using a five-point smoother to reduce the smaller-scale background variability though the overall ray-tracing results are hardly changed with the 30-km unsmoothed model output.

The idealized mesoscale simulations of Z04 were initialized with a balanced two-dimensional (2D) channel baroclinic jet (his Fig. 1) and a balanced three-dimensional (3D) initial perturbation derived from potential vorticity (PV) inversion (Davis and Emanuel 1991). Subsequent evolution of the potential temperature and pressure at the surface and the jet stream level in MM5 simulated the life cycle of a typical extratropical cyclone with clear signals of mesoscale gravity waves at upper levels in the vicinity of the jet-front system persisting for at least 12–24 h (Z04). Figure 1 shows a snapshot of the surface cyclone, upper-tropospheric (8 km) jet stream and low-stratospheric

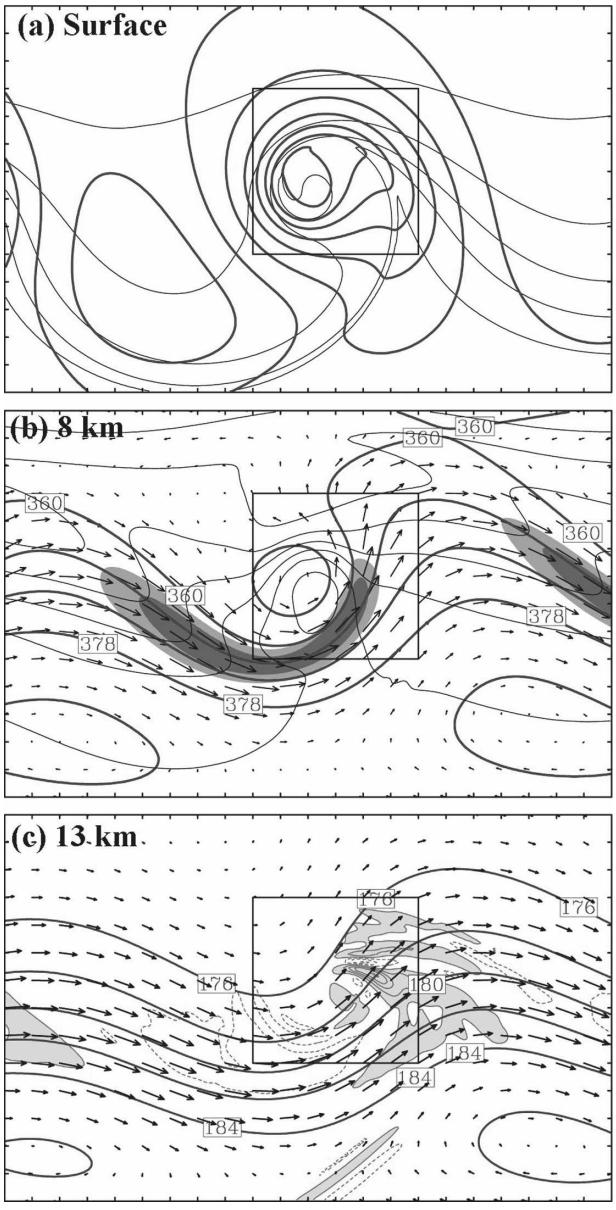

FIG. 1. The control experiment (CNTL) of Z04, showing simulated (a) surface potential temperature (thin line, every 8 K) and sea level pressure (thick line, every 10 hPa); (b) 8-km pressure (thick line, every 5 hPa), potential temperature (thin line, every 8 K), and winds (maximum of 50 m s^{-1}, values greater than 40 shaded, every 5 m s^{-1}); and (c) 13-km pressure (thick line, every 2 hPa), horizontal divergence (thin line—solid and shaded, positive; dashed, negative; every 2×10^{-6} s^{-1}), and wind vectors (maximum of 25 m s^{-1}) valid at 114 h. The inner rectangular box denotes the location of all subsequent figures. The distance between tick marks is 300 km.

(13 km) divergence–convergence flow pattern at 114 h, the primary time on which the current study focuses.

As shown in Fig. 1c, there are several regions of pronounced gravity wave activity at 13 km. The waves of

primary focus in Z04 are those with a predominant horizontal wavelength of ~150 km propagating north-northeastward in the exit region of the upper-tropospheric jet streak just downstream of the trough and upstream of the ridge. Aside from the above group, there are two other groups of waves with an apparent origin near the surface: one is in the deepest trough region penetrating directly through the jet streaks above the ("bent back") surface occluded front, and the other is far to the south of the jet stream above the surface cold front. Although some of the surface frontally forced gravity waves may propagate vertically all the way to the upper atmosphere, direct model output and imbalance diagnosis suggest the jet-exit-region gravity waves are spontaneously generated by the flow imbalance of the upper-tropospheric jet-front systems without direct connection to the surface gravity waves. The surface gravity waves originating directly below the jet-exit region are believed to encounter critical levels (and thus dissipate) in the lower troposphere during their vertical propagation. The mesoscale gravity waves in the exit region of the upper-level jet streaks are consistent with those of past observational studies (Uccellini and Koch 1987).

Although *spontaneous balance adjustment* through the continuous production of flow imbalance from the developing baroclinic wave may lead to the continuous radiation of gravity waves, direct or indirect forcing by the surface fronts cannot be fully ruled out in Z04. The spectral decomposition and ray tracing techniques are thus employed in this study to further differentiate the gravity waves originating at upper levels from those originating near the surface.

4. Wave identification and characteristics from 2D spectral decomposition

The 2D Fourier decomposition is employed here to decompose waves in the 30-km D2 output into three distinct scales: the smaller-scale component with horizontal wavelengths (L_h) less than 210 km, the intermediate-scale component with L_h between 210 and 600 km, and the medium-scale component with L_h greater than 600 km. The spectral decomposition is obtained simply through inversed Fourier transfer of all the 2D Fourier coefficients within a selected range of horizontal wavelengths (zeroing out all other beyond the specified range). The spectral analysis is performed on a subset of D2 output with areal coverage of 7500 by 4200 km (area encompassed by Fig. 1). Note that the 30-km D2 output has direct feedback from the 10-km D3 simulation through two-way nesting.

Figure 2 shows the horizontal distribution of the original and decomposed 13-km vertical velocity at 114 h. As expected, the large-scale component (Fig. 2d) shows clear large-scale descent (ascent) upstream (downstream) of the trough and the jet maximum. There are three clear packets of near-monochromatic, smaller-scale waves ($L_h < 210$ km): one is in the immediate exit region of the jet streak (wave packet 1 or WP1; Fig. 2b), another is in the deep trough region cutting cross the jet streak (wave packet 3 or WP3; Fig. 2c), and the third is to the far south of the jet stream directly above surface cold front (bottom center of Fig. 1c). The spectral decomposition also reveals clear signals of medium-scale ($210 < L_h < 600$ km) gravity waves propagating northeastward (wave packet 2 or WP2; Fig. 2b) in the immediate exit region of the jet streak and to the right of WP1. Although all these waves were discussed in Z04, only the jet-exit-region gravity waves (superposition of WP1 and WP2) were examined in detail therein. Since WP2 waves ($L_h \sim 350$ km) are barely separable from the shorter WP1 waves ($L_h \sim 150$ km) within the original field without spectral filtering, they were not identified separately in Z04. Results from spectral decomposition performed in D2 are qualitatively similar to those performed directly with the 10-km D3 output of the same simulation in Wang and Zhang (2007).

Spectral decomposition allows for better estimation of the propagating characteristics of each wave packet. The horizontal wavelengths of WP1, WP2, and WP3 along the center of the wave packets at 13 km are respectively ~150, 350, and 140 km. Meanwhile, their corresponding ground-based phase speeds averaged from 108 to 114 h are respectively ~2.5, 6.0, and -8.0 m s^{-1}, and the wave vector azimuths are respectively 90°, 55°, and 270° (with respect to 0° due east). The shorter-scale waves above the surface fronts have a horizontal wavelength ~100 km and are always phased tied with the surface cold front (not shown).

5. Source analyses with ray tracing

In this section, GROGRAT—introduced in section 2—is employed to track the origin and propagation of the different lower-stratospheric gravity wave packets identified above. The 6-hourly saved 30-km D2 output was ingested into the ray-tracing model to account for the true 4D (time and space) background variations in the ray tracing. Three locations at 13 km and 114 h along the center of each wave packet (denoted by dots in Figs. 2b,c) are selected as the endpoints of different ray paths from which the ray-tracing model is integrated backward in time (also called reverse ray tracing or backtraced). The input parameters for the initial rays

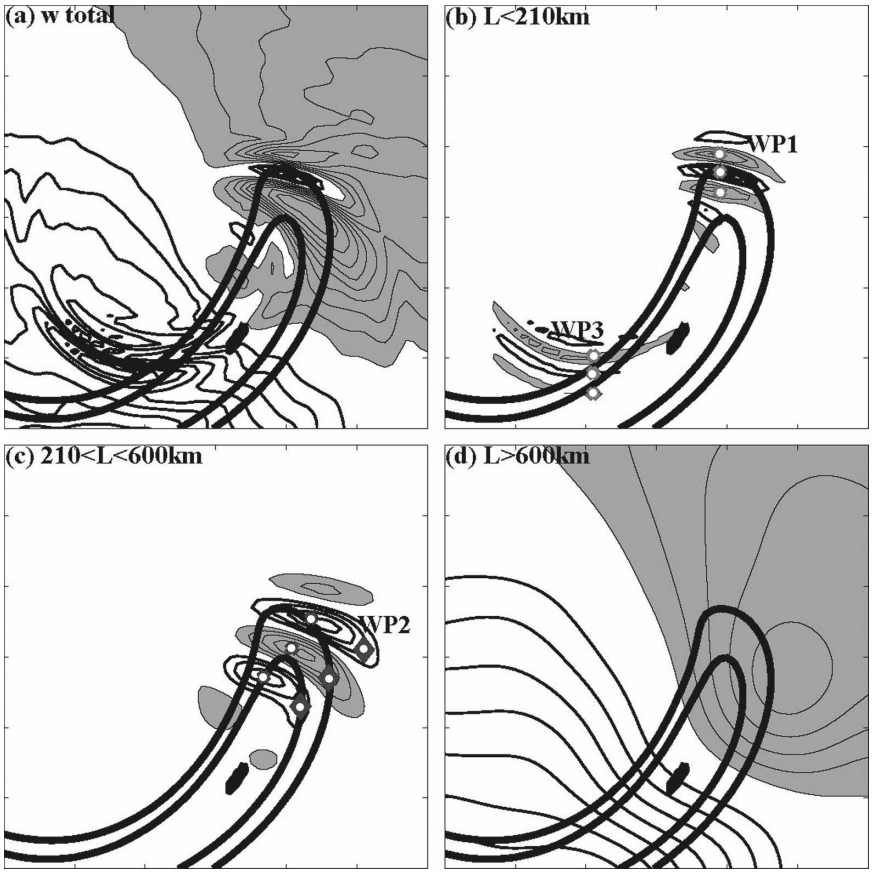

FIG. 2. The CNTL of Z04 simulated 13-km vertical velocity (every 0.0012 m s^{-1}; positive shaded) valid at 114 h for (a) total and the spectral components at different scales for (b) smaller-wavelength $L_h < 210$ km, (c) medium-wavelength $210 < L_h < 600$ km, and (d) larger-wavelength $L_h > 600$ km. Initial backtraced ray positions from WP1 and WP3, whose ray positions are shown in Fig. 4, are denoted in (b) and for WP2 in (c). The 8-km wind speeds (thick lines; >40 m s^{-1}, every 5 m s^{-1}) are plotted to denote the position of the jet.

of each wave group (WP1, WP2, and WP3) are estimated from the 2D spectral decomposition (Table 1). Three additional backtraced rays (denoted by diamonds in Fig. 2c) are computed for WP2 to the east of center of the wave packet.

a. WP1: The shorter-scale gravity waves of $L_h \sim$ 150 km in the jet-exit region

The three backtraced rays launched from WP1 (see Fig. 2b) are denoted as A, B, and C. It is found that all three rays can be traced back to the surface level (ray integration is stopped after rays pass below 1 km). The validity of the WKB index (1), which is essential for the ray-tracing analysis of gravity waves, is examined first. Figure 3 gives the vertical profiles of the WKB index, the vertical gradient of horizontal winds (u and v), and the vertical gradient of the square of buoyancy frequency along the center-ray path of each group. It is found that the WKB index has local peaks right above the jet streaks (due to large vertical wind shear) and in the lower troposphere (due to large variation of static stability) but is always smaller than unity, and thus the WKB approximation remains valid throughout the backward ray integration [Fig. 3a; Eq. (1)].

Although all three rays from WP1 are launched initially at the same time (114 h) and height (13 km), and they can all be traced back to the surface level, the time it takes to propagate through the background atmosphere is different for different rays. The southernmost ray C reaches the bottom of the integration domain (1 km) in a slightly shorter period (3.3 h) than rays A and B (Table 1), mostly due to differences in the lower troposphere.

Next examined are the positions of the rays at different levels and the projection of the rays onto the 2D Fourier decomposition of the shorter-scale component

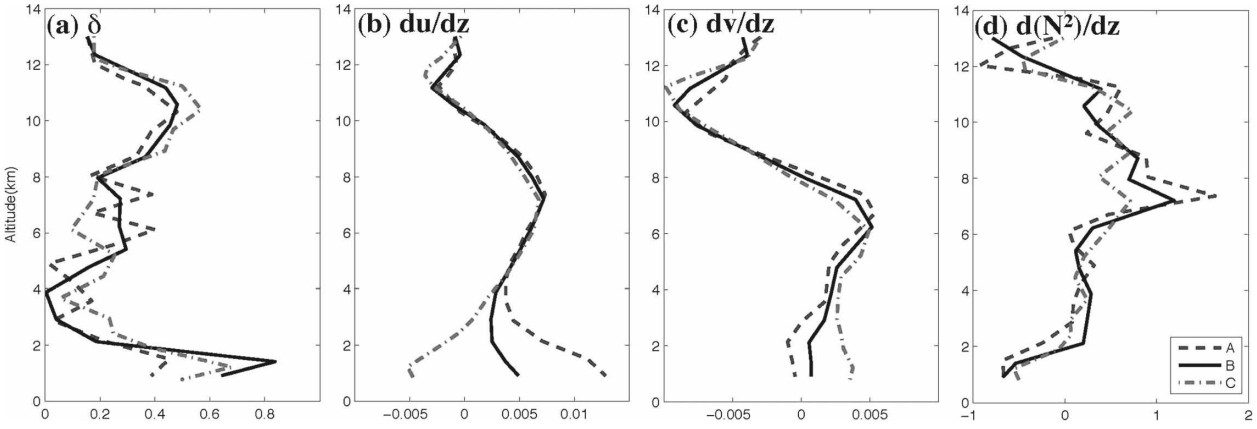

FIG. 3. Vertical profiles of (a) the WKB index δ, and vertical shears of (b) zonal and (c) meridional winds (s^{-1}), and (d) buoyancy frequency (10^{-7} $m^{-1}s^{-2}$) of the three backtraced rays from WP1 (denoted in Fig. 2b) during their backward (and downward) integration.

($L_h < 210$ km) plotted at the closest integer hour to the time the three rays intercept the given levels (Fig. 4). Despite gradually shifting from the center to the right side of the shorter-scale component area (Fig. 4) as they propagated backward in time and downward from 114 h and 13 km, respectively (Fig. 2b), the rays of WP1 generally coincide well with the shorter-wave (~150 km) signals throughout the troposphere. At 1 km, both the filtered shorter-scale component and the rays of WP1 are right atop of the occluded surface fronts (Fig. 4d). This suggests the possibility that shorter-scale WP1 of $L_h \sim 150$ km in the jet-exit region may originate from the lower troposphere near the surface. While gravity wave emission from surface fronts has long been recognized as possible in the literature (e.g., Snyder et al. 1993), this process is not obvious in the direct cross sections of the original model output (Fig. 6c of Z04) and filtered shorter-wave fields (Fig. 10 of Wang and Zhang 2007) because these are not strictly 2D front-forced gravity waves. Along the aforementioned cross sections, the surface, frontally forced gravity waves directly below the jet-exit-region waves are found to encounter a critical level and dissipate before they reach the jet-stream levels.

To further explore the possibility that the shorter horizontal scale, upper-level waves originate near the surface, 11 different forward-integrated rays of shorter scale gravity waves are launched at 108 h all along the

TABLE 1. The starting and termination height (H), time (T), horizontal and vertical wavelength (L_h, L_z), ground-based group velocity in x, y, z directions (c_{gx}, c_{gy}, c_{gz}), and absolute intrinsic frequency ($|\omega^*|$) of the three groups of backtraced rays denoted in Figs. 2b,c.

Ray group		WP1			WP2			WP3		
Ray label		A	B	C	D	E	F	G	H	I
H (km)	Start					13				
	End	0.9	0.9	0.8	3.4	2.9	2.8	0.5	1.0	0.8
T (h)	Start					114				
	End	109.2	110.2	110.7	95.1	96.9	100.8	107.5	108.1	107.6
L_h (km)	Start		150			350			140	
	End	255	195	158	570	551	608	160	116	106
L_z (km)	Start	2.4	2.6	2.8	2.6	2.9	2.8	5.0	5.0	4.9
	End	6.5	9.0	6.9	1.7	1.9	2.7	14.1	9.1	5.4
c_{gx} ($m\ s^{-1}$)	Start	8.6	9.3	9.67	6.7	5.7	7.0	17.1	18.3	19.6
	End	−38.9	−27.0	−12.4	9.1	8.7	13.4	−5.5	4.2	4.7
c_{gy} ($m\ s^{-1}$)	Start	2.8	3	2.93	5.6	5.3	5.8	−7.52	−7.5	−7.5
	End	7.9	6.6	4.8	8.9	8.0	7.3	−11.7	−27.1	−35.6
c_{gz} ($m\ s^{-1}$)	Start	0.13	0.14	0.17	0.06	0.08	0.06	0.53	0.54	0.53
	End	0.38	0.70	0.54	0.01	0.01	0.01	0.79	0.68	0.37
$\|\omega^*\|$ (10^{-4} s^{-1})	Start	3.46	3.69	4.05	1.90	2.01	1.90	6.93	7.02	7.10
	End	3.74	4.80	4.81	1.06	1.09	1.17	3.90	5.06	4.80

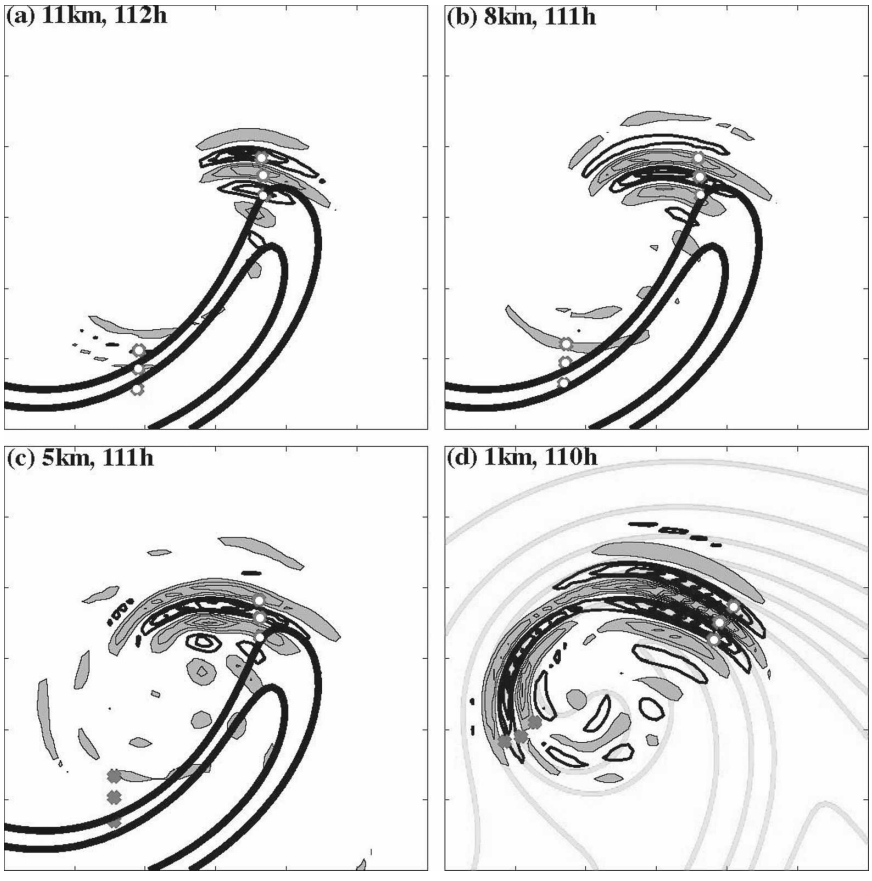

FIG. 4. Positions of different backtraced rays from WP1 and WP3 (initial positions at 13 km and 114 h denoted in Fig. 2b) during their downward integration and the smaller-wavelength ($L_h < 210$ km) spectral component of vertical velocity (positive shaded) at (a) 11, (b) 8, (c) 6, and (d) 1 km valid at the averaged time to the closest integer hour that the three rays of WP1 arrived at that level with every 0.002 m s^{-1} for (a)–(c) and 0.004 m s^{-1} for (d). The 8-km winds >40 m s^{-1} (thick, every 10 m s^{-1}) at 111 h and 1-km potential temperature (thin line, every 4 K) at 110 h are plotted in (d) to denote the position of the jet and the surface fronts.

surface occluded fronts. The initial horizontal wavelength, ground-based horizontal phase speed and wave vector azimuth (derived from the filtered short-wave fields) are respectively ~156 km, ~4.0 m s^{-1}, and ~90° for the seven rightmost rays, and ~156 km, ~6.0, m s^{-1}and ~150° for other four rays. The maximum altitude of all these surface-originating, shorter-wave rays shown in Fig. 5a confirm that not all shorter waves emitted from the surface fronts can propagate into the upper atmosphere (defined here as the 13-km level). Termination of all these rays is due to encountering critical layers. The rays from the region of strongest shorter-wave activity (ray 2 to ray 6 from left to right in Fig. 5) terminate in the low-to-middle troposphere while the rays near the right edge of the strong shorter-wave activity are somewhat similar to the reverse rays (A, B, and C) from WP1 discussed earlier. This again suggests that WP1 may originate from near-surface frontal boundaries. However, neither the backward nor forward ray tracing can rule out the possibility that these shorter waves may completely or partially originate at upper levels. This is because both the forward and backtraced rays pass through the upper tropospheric jet-exit region of maximum imbalance (Z04) and the wave energy source can be anywhere along the ray paths.

To examine the possible excitation of the shorter-scale gravity waves by the upper- tropospheric jet, three shorter-scale forward rays are launched at 9 km and 108 h in the jet-exit region (Fig. 6a). The initial horizontal wavelength, ground-based horizontal phase speed and wave vector azimuth are 160 km, 3.5 m s^{-1}, and 90°, respectively. These rays are integrated with both a negative (upward) and a positive (downward) wavenumber in the vertical direction. For the upward-propagating rays, the horizontal wavelength, vertical

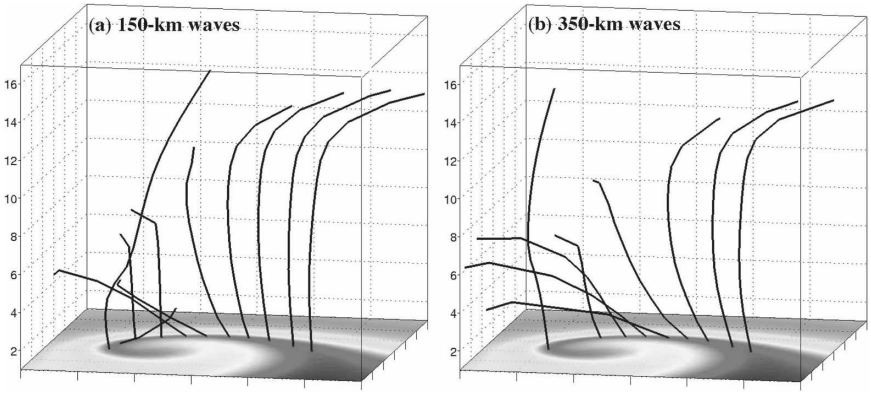

FIG. 5. The 3D display of the ray paths of all forward rays launched at 108 h from the surface fronts with initial wavelengths of (a) 150 and (b) 350 km. The 1-km potential temperature at 108 h is shaded to denote the position of the surface fronts.

wavelength, and intrinsic frequency at 13 km are respectively ~134 km, 1.6 km, and 2.7×10^{-4} s^{-1}. These characteristics are qualitatively similar to those of WP1. Projection of the ray positions onto the corresponding filtered short-wave fields in Fig. 6 further confirms the possibility that WP1 originates from the upper-tropospheric jet-front system as hypothesized in Z04. On the other hand, the downward-propagating rays terminate before reaching the surface due to critical-level filtering.

b. *WP2: The medium-scale gravity waves of $L_h \sim$ 350 km in the jet-exit region*

Here, the three backtraced rays (D, E, and F), whose positions at 13 km and 114 h are denoted with dots in Fig. 2c, are launched from WP2. The ray paths of these medium-scale gravity waves (WP2) differ significantly from those of WP1 (cf. Figs. 6 and 9). With longer wavelengths, the gravity waves along the rays of WP2 have an intrinsic frequency close to the inertial frequency, which is much smaller than that of WP1. None of the rays (D, E, or F) can be traced backward to the surface level; they all terminate at ~3.0 km in the lower troposphere where the vertical group velocity is nearly zero (we used a threshold of 0.0001 m s^{-1} defaulted in GROGRAT) due to a critical level (Table 1).

The ray paths (D, E, and F) of the medium-scale waves are also projected onto the intermediate-scale component of the spectral decomposition in Fig. 7. The rays of WP2 correspond well with the filtered intermediate-scale wave signals at or above the upper-tropospheric jet-front systems (Figs. 7a,b), but the rays no

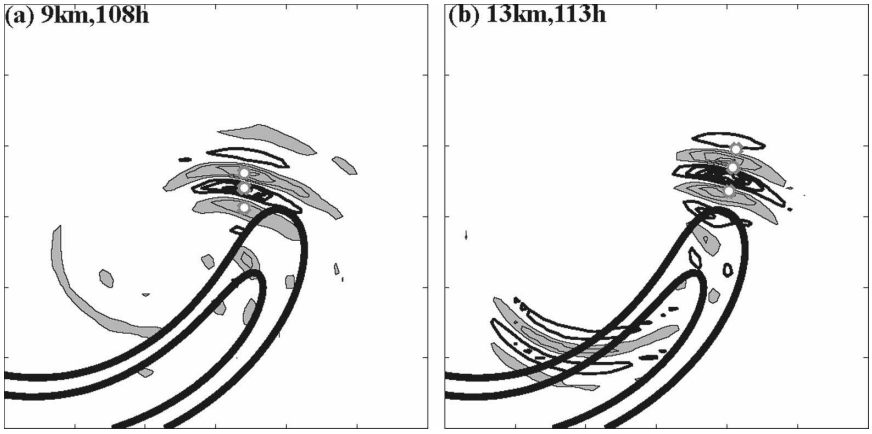

FIG. 6. Positions of the three 150-km rays during their forward (and upward) integration and the smaller-wavelength ($L_h < 210$ km) spectral component of vertical velocity (every 0.001 m s^{-1}; positive shaded) at (a) 9 km and 108 h (initial positions) and (b) 13 km and 113 h (the averaged time to the closest integer hour that the three rays arrived at that level). The 8-km wind speeds (thick line; >40 m s^{-1}, every 5 m s^{-1}) at 108 h are plotted to denote the position of the jet.

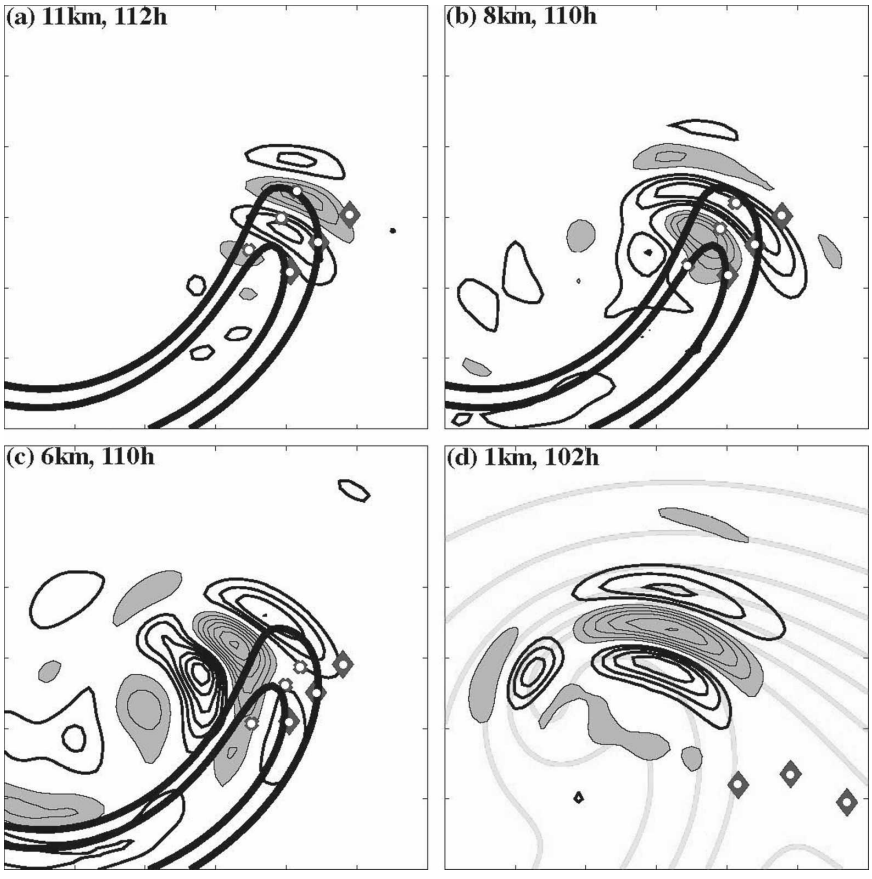

FIG. 7. Positions of the six rays from WP2 (initial position at 13 km and 114 h denoted in Fig. 2c) during its backward (and downward) integration and the medium-wavelength ($210 < L_h < 600$ km) spectral component of vertical velocity (positive shaded) at (a) 11, (b) 8, (c) 6, and (d) 1 km valid at the averaged time to the closest integer hour that the three rays arrived at that level with every 0.002 m s^{-1} for (a)–(c) and 0.004 m s^{-1} for (d). The 8-km wind speeds (thick lines; >40 m s^{-1}, every 5 m s^{-1}) at 111 h and 1-km potential temperature (thick, every 4 K) at 102 h are plotted in (d) to denote the positions of the jet and the surface fronts.

longer overlap with the strong filtered signals below the jet streams (Figs. 7c,d). At the same time, another three rays launched on the southeastern edge of WP2 (also at 13 km and 114 h, denoted with diamonds in Fig. 2c) integrated backward may reach the surface level, but their near-surface locations are far away from the significant medium-scale wave activity associated with the surface occluded fronts (Fig. 7d). The above backward ray tracing of WP2 thus suggests that the medium-scale gravity waves in the jet-exit region most likely originate from the upper-level jet-front systems.

The ray analyses above indicate that there are two packets of medium-scale gravity waves in the exit region of the upper-level jet streaks at 9 km and 108 h. One of these appears to propagate to the north and upward and the other propagates to the northeast and downward (Fig. 8a). Two sets of three rays are launched along the center of each packet at 9 km and 108 h, and the ray-tracing model is then integrated forward in time (initial positions for upward rays Fig. 8a and for downward rays in Fig. 9a). The initial horizontal wavelength, ground-based horizontal phase speed and wave vector azimuth are respectively ~400 km, 3.0 m s^{-1}, and 90° for the upward propagating packet. Subsequent projection of the ray paths onto the filtered intermediate-scale component shows good agreement between the ray-tracing and spectral analysis of the wave signals (Fig. 8b), but the averaged horizontal wavelength of the rays at 13 km is ~260 km, which is much smaller than the typical ~350-km horizontal wavelength of WP2 at this level. Meanwhile, the initial horizontal wavelength, ground-based horizontal phase speed, and wave vector azimuth are chosen to be ~500 km, 5.8 m s^{-1}, and 25° for the downward-propagating packet. Figure 9 shows that the rays for the downward-propagating waves also align well with the filtered medium-scale waves, but

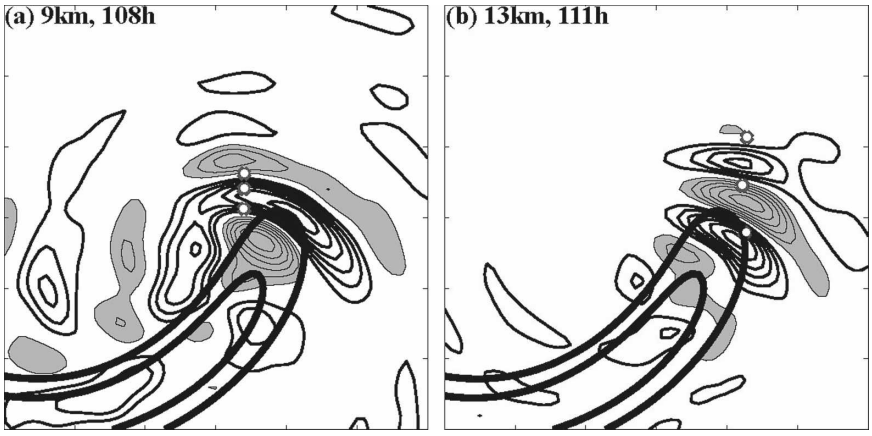

FIG. 8. Positions of the three medium-scale rays during their forward (and upward) integration and the medium-wavelength ($210 < L_h < 600$ km) spectral component of vertical velocity (every 0.001 m s^{-1}; positive shaded) at (a) 9 km and 108 h (initial positions) and (b) 13 km and 111 h (the averaged time to the closest integer hour that the three rays arrived at that level). The 8-km wind speeds (thick line; >40 m s^{-1}, every 5 m s^{-1}) at 108 h are plotted to denote the position of the jet.

downward rays will later stall in the mid-to-lower troposphere. Both the upward and downward rays launched from the jet-exit region further demonstrate that the upper-tropospheric jet-front system is the most likely source region for the medium-scale gravity waves (e.g., WP2).

Since there are also apparent medium-scale gravity waves in the filtered intermediate-scale component near the surface (not shown), 11 medium-scale rays are also launched from the surface frontal regions. These longer-scale rays have the same initial positions as those shorter-scale rays discussed in section 4a (see Fig. 5a). The initial horizontal wavelength, ground-based horizontal phase speed, and wave vector azimuth are respectively ~300 km, 6.0 m s^{-1}, and 80° for the seven rays located right of the occluded surface fronts and ~300 km, −6.0 m s^{-1}, and 150° for the other four rays to the left. Similar to the propagating upward gravity waves with shorter horizontal wavelengths, not all the waves launched from the surface front can propagate into the upper atmosphere. However, three rays at the extreme right end of the group and another at the other leftmost end can propagate to the 13-km level (Fig. 5b). The locations of five rays near the right edge of wave activity coincide approximately with the gravity wave packets at different heights (not shown). The spectral decomposition in combination with forward/backward ray-tracing analyses suggest that the upper jet-frontal systems (where there is maximum imbalance) are the most likely source of WP2, but contributions from the surface frontal systems cannot be entirely ruled out.

c. WP3: The shorter-scale gravity waves of L_h ~ 140 km in the deep trough region

Similarly, the three backtraced rays labeled as G, H, and I are launched from WP3, and their positions at 13 km and 114 h are denoted with dots in Fig. 2a. The ray trajectories of these gravity waves in WP3 all reach the surface level (Fig. 4), but differ significantly from the rays in WP1 and WP2. The backtraced rays gradually shift to the left during their downward propagation without any significant change in wave vector azimuth at or above 5 km (Figs. 4a–c). Below 5 km, the ray paths quickly rotate so that they are aligned across the occluded fronts to the west of the surface cyclone (Fig. 4d) by the time they reach the surface. The ray paths of WP3 also agree well with the forward shorter-wave ray path launched from the extreme west end of the surface occluded fronts discussed in section 5a (Fig. 5). These results show that the gravity waves in WP3 most likely originate from the surface frontal systems.

6. Ray-tracing sensitivity

Horizontal wavelength and ground-based phase speed are two important initial wave parameters in backtraced gravity waves. Since there are inaccuracies in the estimations of the horizontal wavelength and ground-based phase speed in section 4, the sensitivity of the ray-tracing results to initial parameters of the three upper-level wave packets (WP1, WP2, and WP3) is examined. Here, the backward ray tracing is performed as in section 4 with three rays for each packet with the

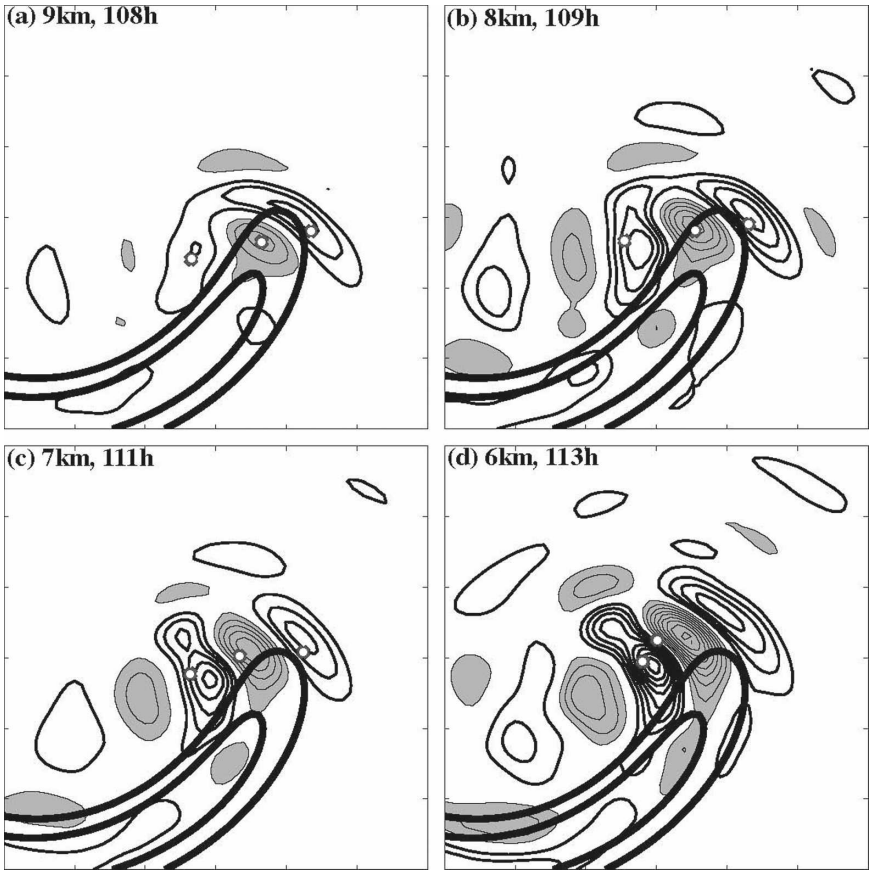

FIG. 9. Tracing of the three forward-tracing 350-km rays during their downward integration and the medium-wavelength ($210 < L_h < 600$ km) spectral component of vertical velocity (positive shaded) for (a) initial position at 9 km and 108 h, and for subsequent positions at (b) 8, (c) 7, and (d) 6 km valid at the averaged time to the closest integer hour the three rays arrived at that level. Contour intervals are every 0.002 m s^{-1} for (a), (b) and 0.004 m s^{-1} for (c), (d). The 8-km wind speeds (thick line; >40 m s^{-1}, every 5 m s^{-1}) at 108 h are plotted to denote the position of the jet.

same initial position and phase speed and direction. However, for each of the rays the initial horizontal wavelengths in WP1 and WP3 vary from 100 to 200 km, and they vary from 300 to 400 km for WP2. For simplicity, hereafter we only show the evolution of the rays located in middle of each group (i.e., B for WP1, E for WP2, and H for WP3).

In Fig. 10, the differences in the profiles of the vertical group velocity and horizontal wavelength are due to the use of different horizontal wavelengths in the backtraced rays (B of WP1, E of WP2, and H of WP3). The rays with shorter initial horizontal wavelengths correspond to a larger vertical group velocity, especially in the vicinity of upper-tropospheric jet streaks. Although the evolution of vertical group velocity, horizontal wavelength (Figs. 10a,b,e,f), and other wave properties are sensitive to the initial wavelength, the shorter-scale rays (B from WP1 and H from WP3) will all reach the bottom of the model domain. Also, despite the larger variations of wave properties in WP2 due to different initial horizontal wavelengths, each of the rays terminates at similar altitude (2–4 km) due to critical-level filtering before reaching the surface (Figs. 10c,d).

In addition to the above tests of sensitivity to horizontal wavelength, the sensitivity of the ray tracing to the initial estimate of the ground-based phase speeds is also tested. Phase speeds are changed from 1.0 to 4.0 m s^{-1} for ray B (WP1), from -6.0 to -8.0 m s^{-1} for H (WP3), and from 4.0 to 8.0 m s^{-1} for E (WP2), while the other initial input parameters are kept the same as in section 5. Despite slight changes in their horizontal position along the downward path (not shown), the intrinsic frequency and vertical group velocity of each ray are both largely insensitive to the difference in initial phase speed (not shown).

Variations in the background flow are shown to be

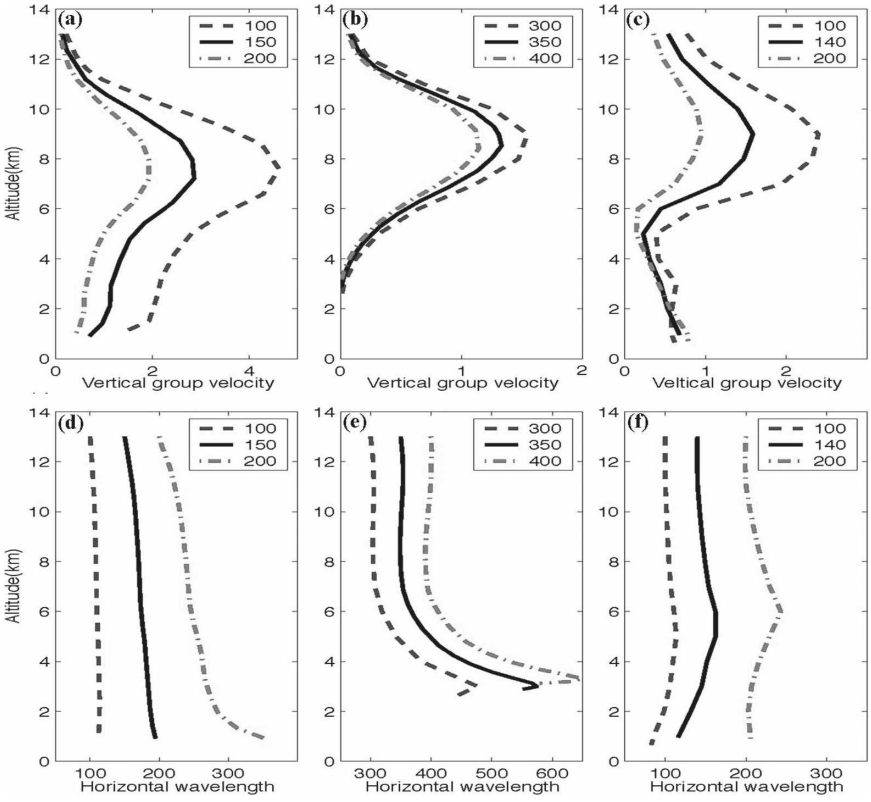

FIG. 10. Sensitivity of (top) vertical group velocity (10^{-2} m s^{-1}) and (bottom) horizontal wavelength (km) of the backtraced rays to the use of different initial horizontal wavelengths: (a), (d) 100, 150, and 200 km for ray B; (b), (e) 300, 350, and 400 km for ray E; and (c), (f) 100, 140, and 200 km for ray H.

significant in the ray paths, and since the time resolution of model output for the above ray-tracing experiments is rather coarse (6 h), another set of ray-tracing sensitivity experiments is performed by updating the background fields every 3 h. Comparison of the group velocity profile for rays representing WP1, WP2, and WP3 shows that changing the data interval from 6 to 3 h makes almost no noticeable difference in the ray paths (not shown). This further indicates that the change in the background is much slower than the variations of the gravity waves (a further assurance that the WKB assumption is valid). No significant changes in ray paths are found when even higher resolution model output (in both time and space) is used (not shown).

7. Summary and discussion

Using a two-dimensional Fourier decomposition and a four-dimensional ray-tracing technique, this study investigates the group propagation characteristics and possible source mechanisms of mesoscale gravity waves simulated in the idealized baroclinic jet-front system of Z04.

The two-dimensional Fourier decomposition successfully separates the simulated gravity waves from the complex background flow in the troposphere and lower stratosphere. Four distinct groups of gravity waves identified from the decomposition are investigated. One is a northward-propagating wave packet with a horizontal wavelength of ~150 km in the immediate exit region of the jet streak (WP1), and another has a horizontal wavelength of ~140 km and a horizontal wave vector veering from northward to southward in the deep trough region cutting across the jet streak (WP3). The third has a horizontal wavelength of ~350 km and propagates northeastward (WP2), also in the immediate exit region of the jet streak but to the right of WP1. The medium-scale gravity waves in WP2 are barely separable from WP1 in the original field examined in Z04. The fourth group to the far south of the jet right above the surface cold front with horizontal wavelengths of ~100–150 km is clearly generated by the surface fronts.

Ray-tracing analysis suggests that the medium-scale gravity waves (WP2) originate from the upper-tropospheric jet-front system (where there is maximum imbalance), though contributions from the surface fronts cannot be completely ruled out. The shorter-scale gravity waves (WP3) in the deep trough region penetrating across the jet streak most likely initiate from the surface frontal system. The jet-exit-region, northward-propagating, shorter gravity waves (WP1), on the other hand, may originate from either the upper-tropospheric jet-front system or the surface frontal system.

Ray-tracing analysis also reveals a very strong influence of the spatial and temporal variability of the complex background flow (and associated background deformation) on the characteristics of gravity waves as they propagate. Nevertheless, our ray-tracing analyses and spectral decomposition suggest the "wave capturing" theory proposed by Bühler and McIntyre (2005) and applied in Plougonven and Snyder (2005) appears to be insufficient to explain the gravity wave patterns in the jet-exit region, since 1) these mesoscale waves obviously have different wave characteristics and aspect ratios at this same region and 2) significant vertical group propagation of the rays will propagate the waves away before the background deformation has sufficient time to "capture" the waves. Strong variations in the wave characteristics and background flow as well as collocation of waves with different characteristics will certainly lead to difficulties in using individual sounding-based hodograph methods to accurately retrieve the gravity wave properties (e.g., Eckermann 1996; Zhang et al. 2004).

It is also worth noting that, for both forward and backward ray tracing examined in this study, the gravity wave parameters such as horizontal wavelengths from the ray-tracing analysis are slightly less than those estimated directly from the 2D spectral decomposition. The positioning of the rays, especially those of longer waves, may also be slightly shifted from that derived from the 2D decomposition. These discrepancies may come from the omission of both horizontal and vertical shears in the ray calculation and the rapid spatial variation of the background environment despite the satisfaction of the WKB criteria in the ray-tracing analysis.

Acknowledgments. Thanks are due to Steve Eckermann for providing codes and help on the GROGRAT model. Discussions with and comments from Eckermann, Tim Dunkerton, Chris Snyder, Todd Lane, Craig Epifanio, and Riwal Plougonven are helpful. We are also grateful to Shuguang Wang for his help on figures, and to Jason Sippel and Wang for their proofreading of earlier versions of the manuscript. Most of this study was conducted during YL's sabbatical visit at Texas A&M University. The research was supported by the NSF Grants ATM-0203238 and ATM-0618662 and by the China 973 Project under Grant 2004CB418304.

REFERENCES

Broutman, D., 1984: The focusing of short internal waves by an inertial wave. *Geophys. Astrophys. Fluid Dyn.,* **30,** 199–225.

——, J. W. Rottman, and S. D. Eckermann, 2001: A hybrid method for analyzing wave propagation from a localized source, with application to mountain waves. *Quart. J. Roy. Meteor. Soc.,* **127,** 129–146.

Bühler, O., and M. E. McIntyre, 2005: Wave capture and wave-vortex duality. *J. Fluid Mech.,* **534,** 67–95.

Davis, C. A., and K. A. Emanuel, 1991: Potential vorticity diagnosis of cyclogenesis.. *Mon. Wea. Rev.,* **119,** 1929–1952.

Dunkerton, T. J., and N. Butchart, 1984: Propagation and selective transmission of inertial gravity waves in a sudden warming. *J. Atmos. Sci.,* **41,** 1443–1460.

Eckermann, S. D., 1992: Ray-tracing simulation of the global propagation of inertia gravity waves through the zonally averaged middle atmosphere. *J. Geophys. Res.,* **97,** 15 849–l5 866.

——, 1996: Hodographic analysis of gravity waves: Relationships among Stokes parameters, rotary spectra, and cross-spectral methods. *J. Geophys. Res.,* **101,** 19 169–19 174.

——, and C. J. Marks, 1997: GROGRAT: A new model of the global propagation and dissipation of atmospheric gravity waves. *Adv. Space Res.,* **20,** 1253–1256.

Fritts, D. C., and M. J. Alexander, 2003: Gravity wave dynamics and effects in the middle atmosphere. *Rev. Geophys.,* **41,** 1003, doi:10.1029/2001RG000106.

Gerrard, A. J., T. J. Kane, S. D. Eckermann, and J. P. Thayer, 2004: Gravity waves and mesospheric clouds in the summer middle atmosphere: A comparison of lidar measurements and ray modeling of gravity waves over Sondrestrom, Greenland. *J. Geophys. Res.,* **109,** D10103, doi:10.1029/2002JD002783.

Griffiths, M., and M. J. Reeder, 1996: Stratospheric inertia-gravity waves generated in a numerical model of frontogenesis. I: Model solutions. *Quart. J. Roy. Meteor. Soc.,* **122,** 1153–1174.

Guest, F. M., M. J. Reeder, C. J. Marks, and D. J. Karoly, 2000: Inertia-gravity waves observed in the lower stratosphere over Macquarie Island. *J. Atmos. Sci.,* **57,** 737–752.

Holton, J. R., and M. J. Alexander, 2000: The role of waves in the transport circulation of the middle atmosphere. *Atmospheric Science across the Stratopause, Geophys. Monogr.,* Vol. 130, Amer. Geophys. Union, 21–35.

Hooke, W. H., 1986: Gravity waves. *Mesoscale Meteorology and Forecasting,* P. S. Ray, Ed., Amer. Meteor. Soc., 272–288.

Jones, W. L., 1969: Ray tracing for internal gravity waves. *J. Geophys. Res.,* **74,** 2028–2033.

Koch, S. E., and Coauthors, 2005: Turbulence and gravity waves within an upper-level front. *J. Atmos. Sci.,* **62,** 3885–3908.

Lane, T. P., J. D. Doyle, R. Plougonven, M. A. Shapiro, and R. D. Sharman, 2004: Observations and numerical simulations of inertia gravity waves and shearing instabilities in the vicinity of a jet stream. *J. Atmos. Sci.,* **61,** 2692–2706.

Lighthill, M. J., 1978: *Waves in Fluids*. Cambridge University Press, 504 pp.

Marks, C. J., and S. D. Eckermann, 1995: A three-dimensional nonhydrostatic ray-tracing model for gravity waves: Formulation and preliminary results for the middle atmosphere. *J. Atmos. Sci.,* **52,** 1959–1984.

O'Sullivan, D., and T. J. Dunkerton, 1995: Generation of inertia-gravity waves in a simulated life cycle of baroclinic instability. *J. Atmos. Sci.,* **52,** 3695–3716.

Plougonven, R., and C. Snyder, 2005: Gravity waves excited by jets: Propagation versus generation. *Geophys. Res. Lett.,* **32,** L18802, doi:10.1029/2005GL023730.

——, and F. Zhang, 2007: On the forcing of inertia–gravity waves by synoptic-scale flows. *J. Atmos. Sci.,* **64,** 1737–1742.

Snyder, C., W. C. Skamarock, and R. Rotunno, 1993: Frontal dynamics near and following frontal collapse. *J. Atmos. Sci.,* **50,** 3194–3211.

Uccellini, L. W., and S. E. Koch, 1987: The synoptic setting and possible source mechanisms for mesoscale gravity wave events. *Mon. Wea. Rev.,* **115,** 721–729.

Wang, S., and F. Zhang, 2007: Sensitivity of mesoscale gravity waves to the baroclinicity of jet-front systems. *Mon. Wea. Rev.,* **135,** 670–688.

Zhang, F., 2004: Generation of mesoscale gravity waves in upper-tropospheric jet-front systems. *J. Atmos. Sci.,* **61,** 440–457.

——, S. E. Koch, C. A. Davis, and M. L. Kaplan, 2001: Wavelet analysis and the governing dynamics of a large-amplitude gravity wave event along the east coast of the United States. *Quart. J. Roy. Meteor. Soc.,* **127,** 2209–2245.

——, S. Wang, and R. Plougonven, 2004: Potential uncertainties in using the hodograph method to retrieve gravity wave characteristics from individual soundings. *Geophys. Res. Lett.,* **31,** L11110, doi:10.1029/2004GL019841.